

3DStokesFlow: simulation-based inference for 3D Stokes profiles using flow matching

A. Asensio Ramos^{1,2}, Kai E. Yang³, M. J. Martínez González^{1,2}, S. Curt Dodds⁵, Xudong Sun⁴

¹ Instituto de Astrofísica de Canarias (IAC), Avda Vía Láctea S/N, 38200 La Laguna, Tenerife, Spain
e-mail: andres.asensio@iac.es

² Departamento de Astrofísica, Universidad de La Laguna, 38205 La Laguna, Tenerife, Spain

³ SETI Institute, Mountain View, CA 94043, USA

⁴ Institute for Astronomy, University of Hawai'i at Mānoa, Pukalani, HI 96768, USA

⁵ Institute for Astronomy, University of Hawai'i at Mānoa, Honolulu, HI 96822, USA

Received ; accepted

ABSTRACT

Context. The standard interpretation of observed Stokes profiles to infer the physical conditions of the solar atmosphere is inherently an ill-defined problem due to observational noise and mathematical degeneracies. Traditional pixel-by-pixel (1D) inversion codes provide point estimates with unreliable uncertainties, at the expense of significant computational time. Recent machine-learning-based Bayesian frameworks are restricted to 1D spatial configurations, ignoring crucial spatial correlations between neighboring pixels.

Aims. We aim to develop a novel multidimensional inversion framework capable of performing fast and scalable Bayesian inference across an entire 2D field-of-view (FoV). This approach seeks to provide accurate height-dependent atmospheric parameters with reliable posterior distributions while exploiting spatial correlations.

Methods. We introduce a new generative modeling strategy based on conditional flow matching. The model utilizes multi-scale spatial features extracted from observed Stokes profiles in the Fe I line pair at 630 nm, which then conditions a flow matching generative model to sample from the complex posterior distribution of the atmospheric parameters. The framework is trained using realistic 3D quiet Sun magnetohydrodynamic simulations.

Results. Validation on independent synthetic datasets demonstrates that the model accurately captures the true 3D stratification of all thermodynamic and magnetic parameters. Because the code additionally provides a geometrical height scale, it allows for the computation of 3D electric current density maps, Lorentz forces, and Ohmic and ambipolar dissipation maps in the solar photosphere. Application to real Hinode/SP quiet Sun observations yields highly localized electric currents at magnetic boundaries. We also leverage the 3D geometrical information to trace the emergence of small-scale emerging magnetic loops across the solar atmosphere.

Key words. Methods: numerical, data analysis — techniques: polarimetric — Sun: photosphere, magnetic fields

1. Introduction

The interpretation of observed Stokes profiles to obtain information about the physical conditions of the solar atmosphere is routinely performed with inversion codes (del Toro Iniesta & Ruiz Cobo 2016; de la Cruz Rodríguez & van Noort 2017). These codes are based on the iterative modification of atmospheric models so that the synthetic Stokes profiles emerging from the model atmosphere match the observed ones. Different spectral lines require different levels of complexity in the forward modeling. The simplest codes assume a Milne-Eddington (ME) atmosphere (Auer et al. 1977; Landi Degl'Innocenti & Landolfi 2004), where gradients along the line-of-sight (LOS) are not relevant. Codes like MERLIN (Lites et al. 2007), MILOS (Orozco Suárez & Del Toro Iniesta 2007), VFISV (Borrero et al. 2011), and pyMilne (de la Cruz Rodríguez 2019) work under this assumption and are, on average, very fast. When gradients are relevant, the inversion requires the prescription of a stratification of the physical parameters with height. If the lines can be safely assumed to form under the local thermodynamic equilibrium (LTE) approximation, the forward modeling is relatively simple and fast. Consequently, several codes have

been developed to perform inversions under this assumption. Starting with the seminal work of Ruiz Cobo & del Toro Iniesta (1992) and the development of SIR, a handful of codes are now available, including SPINOR (Frutiger et al. 2000), FIRTEZ (Pastor Yabar et al. 2019), and SPINOR-2D (van Noort 2012). More complex non-LTE line formation is required for the inversion of chromospheric lines. These approaches need to consistently solve the radiative transfer equation and the statistical equilibrium equations at each iteration of the inversion process. These codes are much more complex and computationally demanding, and only a few are available to the community: NICOLE (Socas-Navarro et al. 2015), STiC (de la Cruz Rodríguez et al. 2019), SNAPi (Milić & van Noort 2018), DeSIRE (Ruiz Cobo et al. 2022), and TIC (Li et al. 2022).

Despite all the efforts carried out in recent decades, it is important to note that the inversion of Stokes profiles remains an ill-defined problem. This is not just a consequence of potential mathematical degeneracies in the forward modeling (such as the well-known 180° ambiguity in the azimuth of the magnetic field), in which identical Stokes profiles can be produced by different atmospheric models. The presence of noise in observa-

tions also induces non-unique solutions, producing uncertainties in the inferred atmospheric parameters. Standard inversion codes often provide a point estimate of the final covariance matrix at the solution (e.g., see [Ruiz Cobo & del Toro Iniesta 1992](#)), but the inferred uncertainties obtained from this covariance matrix tend to be unreliable because they are calculated purely based on the goodness of the fit and the parameter sensitivity of the problem. For this reason, strictly speaking, the inversion of Stokes profiles must be treated as a probabilistic inference problem. The goal is to characterize the posterior distribution of the atmospheric parameters given the observed Stokes profiles. This was first attempted by [Asensio Ramos et al. \(2007\)](#) using a Markov Chain Monte Carlo (MCMC) method under the assumption of a ME atmosphere. Given that this approach is computationally demanding, it has been difficult to extend it to more complex atmospheres.

Only recently, with the advent of machine learning techniques, has it been possible to perform Bayesian inference in more complex atmospheres. The first attempt was performed by [Osborne et al. \(2019\)](#), who used invertible neural networks ([Ardizzone et al. 2018](#)) to capture degeneracies and uncertainties when inverting Stokes profiles from flaring regions. More recently, [Díaz Baso et al. \(2022\)](#) used normalizing flows to provide extremely fast variational approximations to the posterior distribution in lines formed in LTE and non-LTE. [Mistryukova et al. \(2023\)](#) trained a neural model to provide a Gaussian variational approximation to the posterior distribution, while [Xu et al. \(2024\)](#) trained emulators to accelerate the forward modeling and then used MCMC methods to sample the posterior distribution. Finally, the latest effort in this direction was presented by [Asensio Ramos & de la Cruz Rodríguez \(2025\)](#), who treated inversions as a neural translation problem and trained a model to directly map Stokes profiles to atmospheric parameters in a generative fashion, thereby providing a variational approximation to the posterior distribution.

All the variational approximations mentioned above are currently limited to 1D model atmospheres. However, it is becoming increasingly clear that exploiting the spatial correlation between neighboring pixels is crucial to obtaining more accurate and reliable inferences ([Asensio Ramos & Díaz Baso 2019](#); [Yang et al. 2024](#)). Given the dimensionality of the resulting posterior distribution when inverting 2D FoVs, performing Bayesian inference in this case is an extremely challenging problem. The dimensionality of the problem grows with the number of pixels multiplied by the depth stratification of all physical parameters. For instance, a 2D map of 100×100 pixels with a depth stratification of 10 points for temperature, LOS velocity, and the three cartesian components of the magnetic field, results in a posterior distribution of dimension $5 \times 10 \times 100 \times 100$, i.e., half a million dimensions.

In this work, we take full advantage of recent advances in generative modeling to propose a novel strategy based on flow matching to perform Bayesian inference of atmospheric parameters from Stokes profiles. This method exploits the spatial correlation between neighboring pixels and can provide accurate inferences and uncertainties for the atmospheric parameters across the entire observed FoV. Apart from a significant improvement in terms of speed, the exploitation of spatial correlation allows us to obtain information regarding geometrical height and gas pressure. This opens up the possibility of using very simple disambiguation methods for the transverse components of the magnetic field, which allows us to calculate electric current density maps. From this information, we demonstrate that it is possible

to obtain maps of the ohmic and ambipolar dissipation in the photosphere purely from observations¹.

2. Bayesian Inference via Flow Matching

2.1. Bayesian Inference for Stokes profiles inversion

The inference of the atmospheric parameters from a 2D FoV of observed Stokes profiles can be framed as a Bayesian inference problem. Let us denote by $P \in \mathbb{R}^{N \times d}$ the high-dimensional vector that contains the atmospheric parameters (of dimension d) for each of the N pixels across the entire FoV. We observe the Stokes profiles of some selected spectral lines and denote them by $S \in \mathbb{R}^{N \times m}$, where m denotes the product of all sampled wavelength points across the four Stokes parameters. The goal is to characterize the posterior distribution $p(P|S)$, which captures all the information about the atmospheric parameters given the observed data. The Bayes theorem allows us to express this posterior distribution as:

$$p(P|S) = \frac{p(S|P)p(P)}{p(S)}, \quad (1)$$

where $p(S|P)$ is the likelihood function that captures the forward modeling of the Stokes profiles given the atmospheric parameters, $p(P)$ is the prior distribution that encodes our prior knowledge about the atmospheric parameters, and $p(S)$ is the evidence that serves as a normalization constant.

From a generative modeling perspective, one can solve the Bayesian inference problem by drawing samples from the complex, unknown posterior distribution $p(P|S)$. However, having access to the posterior distribution is, in general, intractable. On one hand, the likelihood function $p(S|P)$ is complex and computationally expensive to evaluate, especially when the forward modeling involves solving the radiative transfer equation under non-LTE conditions. On the other hand, the prior distribution $p(P)$ (models compatible with those one could find in the Sun) can also be difficult to specify accurately, given the high dimensionality of the parameter space and the potential correlations between parameters. However, if one has access to a finite dataset of pairs of atmospheric parameters and their corresponding Stokes profiles, $\{(P_i, S_i)\}_{i=1}^N$, drawn from the joint distribution $p(P, S)$, one can leverage this dataset to learn a generative model that approximates the posterior distribution. Such dataset can simply be generated using simulations, i.e., by running a forward model (e.g., an LTE or non-LTE radiative transfer code) on a set of atmospheric models that are representative of the solar atmosphere.

2.2. Flow Matching

Flow models ([Lipman et al. 2024](#)) are generative models that learn a continuous transformation (or flow) that maps a simple base multivariate distribution (e.g., a standard Gaussian $\mathcal{N}(0, I)$, with I being the identity matrix) to a complex target distribution. Let us denote by $x \in \mathbb{R}^M$ a random variable that follows the base distribution. One can define a time-dependent probability density path p_t for an auxiliary time $t \in [0, 1]$, where p_0 (at $t = 0$) is the tractable base distribution and p_1 (for $t = 1$) is the target posterior distribution. The flow $\psi_t(x)$ is a time-dependent mapping that transports samples $X_0 \sim p_0$ from the base distribution to the target distribution, so that $X_1 \sim p_1$. In general, the trajectory followed by a sample X_0 under the flow can be expressed

¹ <https://asensio.github.io/3dstokesflow>

as $X_t = \psi_t(X_0)$. The distribution of all samples generated by the flow at any arbitrary time t are, therefore, distributed according to the distribution p_t (i.e., $X_t \sim p_t$).

Instead of directly learning the flow $\psi_t(x)$, it is more common to learn the underlying vector field $u_t(x)$ that generates the flow, according to the following ordinary differential equation:

$$\frac{d}{dt}\psi_t(x) = u_t(x), \quad \psi_0(x) = x. \quad (2)$$

The goal of flow matching is to learn a parameterized function $v_t^\theta(x)$, typically given as a sufficiently capable neural network, that generates a flow that produces a probability path p_t from p_0 to p_1 . The ideal objective would be to directly minimize the expected mean squared error between our neural vector field and the true target vector field:

$$\mathcal{L}_{FM}(\theta) = \mathbb{E}_{t, X_t} \left\| v_t^\theta(X_t) - u_t(X_t) \right\|^2, \quad t \sim \pi(t), X_t \sim p_t \quad (3)$$

where $u_t(x)$ is the true target vector field that generates the probability path p_t . The expectation is taken over the time t , which is sampled from the interval $[0, 1]$ with probability $\pi(t)$, and over the samples X_t drawn from the distribution p_t . The main problem of this approach is that we do not have direct access to the true target vector field $u_t(x)$ because it is, indeed, dependent on the intractable transformation between the base distribution and the complex posterior distribution.

To bypass this intractability, Lipman et al. (2024) used a strategy based on analyzing what happens if the target distribution is given by a Dirac delta distribution centered at a single data point X_1 (i.e., $p_1(x) = \delta_{x_1}(x)$). In other words, they analyzed the case conditional on a single data point X_1 . Of all the possible paths that can transport the base distribution to this Dirac delta target distribution, we choose the one that is given by the optimal transport (OT) between the two distributions. This allows us to define the simple and linear path such that $X_t = (1-t)X_0 + tX_1$, where $X_0 \sim p_0$ is a sample drawn from the base distribution (from a practical point of view, we use samples from the standard normal distribution, so that $p_0 = \mathcal{N}(0, I)$). According to Eq. (2), the vector field that generates this path can be easily calculated as:

$$u_t(x|X_1) = X_1 - X_0. \quad (4)$$

This vector field is constant in time and points directly from the sample X_0 to the target sample X_1 . Once trained, the flow generated by this vector field is a straight line between the point X_0 and the data point X_1 , also known as the optimal transport path between the two distributions. The full loss function for this conditional flow matching strategy can be obtained by averaging over the data distribution p_1 and all intermediate points X_t along the path, resulting in:

$$\mathcal{L}_{CFM}(\theta) = \mathbb{E}_{t, X_1, X_t} \left\| v_t^\theta(X_t) - u_t(X_t|X_1) \right\|^2, \quad t \sim \pi(t), X_1 \sim p_1, X_0 \sim p_0, X_t \sim p_t. \quad (5)$$

Using Eq. (4), the conditional loss can be finally rewritten as:

$$\mathcal{L}_{CFM}(\theta) = \mathbb{E}_{t, X_1, X_0} \left\| v_t^\theta(X_t) - (X_1 - X_0) \right\|^2, \quad t \sim \pi(t), X_1 \sim p_1, X_0 \sim p_0. \quad (6)$$

Lipman et al. (2024) showed that this construction via conditional flow matching gives a deceptively simple loss function which is equivalent to minimizing the original flow matching

loss $\mathcal{L}_{FM}(\theta)$. Consequently, the model $v_t^\theta(x)$, trained by optimizing Eq. (6), approximates the true target vector field $u_t(x)$, without ever having direct access to it. Training then proceeds by sampling a data point X_1 from the target distribution, sampling a noise point X_0 from the base distribution, and sampling a time step t from the $\pi(t)$ distribution². The intermediate point X_t is then calculated as $X_t = (1-t)X_0 + tX_1$, and the loss is computed against the known vector field $X_1 - X_0$.

The selection of the pair (X_0, X_1) is often relevant for ending up with an efficient model. The selection is done via a user-defined joint distribution $\pi(X_0, X_1)$, known as the coupling. The simplest case is to select X_0 and X_1 independently from their respective distributions, so that the coupling factorizes as $\pi(X_0, X_1) = \pi(X_0)\pi(X_1)$. In this case, it is likely that the path between X_0 and X_1 will intersect with the paths of other data points, which can make the learning task more difficult for the neural network. Although solutions to end up with non-intersecting paths have been proposed in the literature (such as using a coupling that enforces optimal transport), we have found great results simply picking uniformly random samples from p_0 and p_1 . In other words, we choose $X_0 \sim \mathcal{N}(0, I)$ and X_1 at random from the training set.

2.3. External Conditioning

The velocity model $v_t^\theta(x)$ can be easily extended to include additional conditioning information. In the context of Bayesian inference for Stokes profiles inversion, one can train a flow matching model to compute the posterior distribution of the atmospheric parameters conditioned on the observed Stokes profiles by optimizing the following loss function:

$$\mathcal{L}_{CFM}(\theta) = \mathbb{E}_{t, X_0, (P, S)} \left\| v_t^\theta(X_t, S) - (P - X_0) \right\|^2, \quad t \sim \pi(t), (P, S) \sim p(P, S), X_0 \sim p_0, \quad (7)$$

where the pair (P, S) is drawn from the joint distribution of atmospheric parameters and Stokes profiles.

2.4. Inference

When the model is trained, inference can be performed by sampling from the base distribution and then integrating the learned vector field conditioned on the context S to transport the sample from the base distribution to the target distribution:

$$P = X_0 + \int_0^1 v_t^\theta(X_t, S) dt. \quad (8)$$

This can be achieved by using any off-the-shelf ODE solver and, given that the probability paths are smooth, it can be done with a small number of function evaluations, making the inference process very efficient.

3. Training

3.1. Training data

We train the model with the quiet Sun simulations presented in the SPIN4D³ project (Yang et al. 2024; Yang et al. 2025). These simulations were performed with the MURaM code

² In this work, we use a uniform distribution over $[0, 1]$, so that $\pi(t) = \mathcal{U}(0, 1)$

³ <https://ifauh.github.io/SPIN4D>

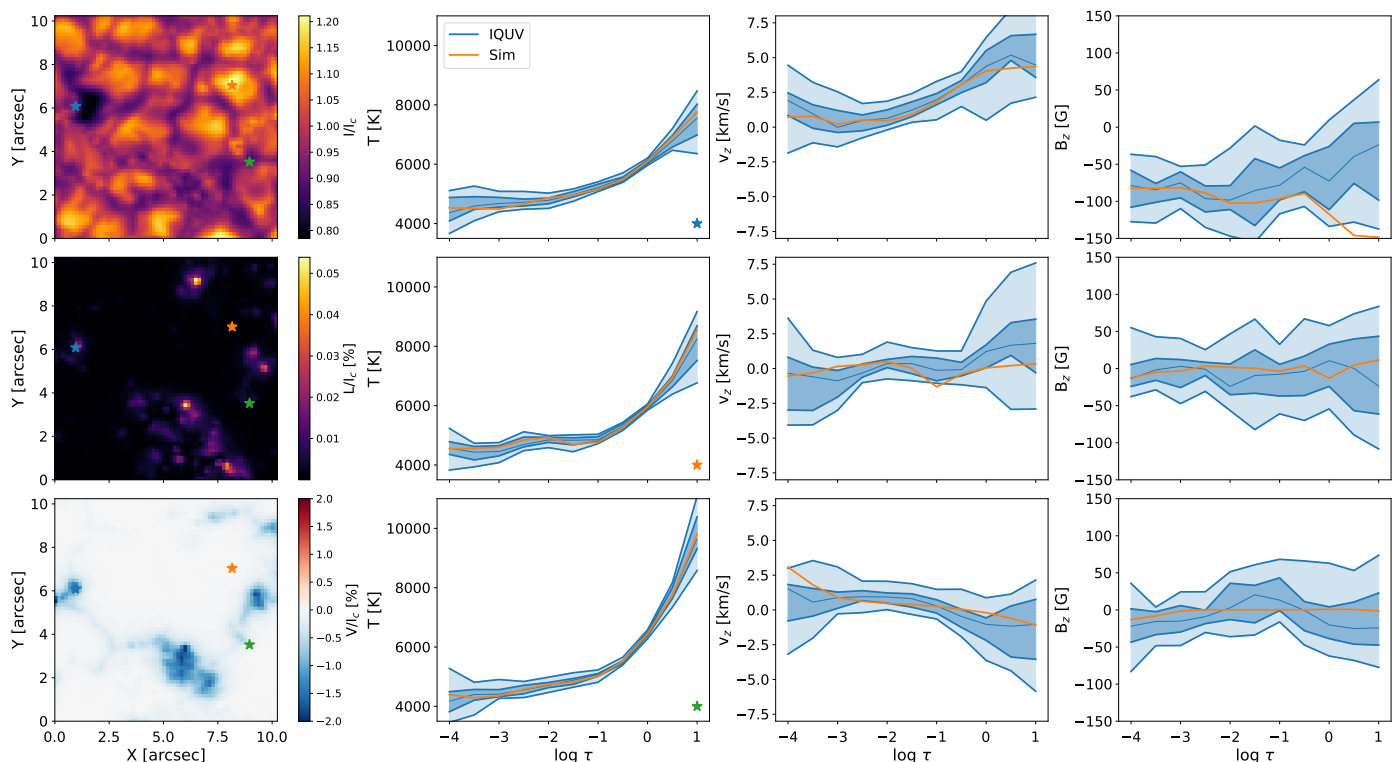


Fig. 1: Vertical cuts of the inferred atmospheric parameters (temperature, LOS velocity, and vertical magnetic field) for three columns of the validation snapshot (each row shows a different pixel). The true values from the simulation are shown in orange, while the median of the posterior distribution is shown in thin blue curves. The shaded areas correspond to the intervals between the 25th and 75th percentile (dark blue) and the 5th and 95th percentiles (light blue) of the posterior distribution.

(Vögler et al. 2005; Rempel et al. 2009; Rempel 2012, 2014), taking the quiet Sun simulation of Rempel (2014) as the initial condition and evolving them after adding different magnetic fields to produce snapshots from very quiet Sun to strong plages. The six initial magnetic configurations considered in this work are: i) zero magnetic field, ii) vertical field with 50 G, iii) inclined fields with 50 G in each cartesian component, iv) vertical field with 100 G, v) vertical field with 200 G, vi) vertical fields of 200 G, -150 G and -50 G added to three quadrants of the simulation box to mimic mix polarities see (see Yang et al. 2024, for more details on the simulations). The first five configurations are used for training, while the sixth one with mixed polarities is used for validation and testing. The horizontal simulation pixel is 16 km and spans 24.6×24.6 Mm horizontally. Snapshots every 12 min are considered, resulting in roughly 30 snapshots per simulation. A second set of snapshots is obtained by flipping the sign of the magnetic field vector, to avoid potential biases in the training data.

The snapshots contain the vertical stratification of the atmospheric parameters as a function of position on the 2D grid. We consider the temperature T , LOS velocity v , the gas pressure P , and the three cartesian components of the magnetic field $\mathbf{B} = (B_x, B_y, B_z)$. The 180° ambiguity in the transverse components of the magnetic field is avoided (Asensio Ramos & Díaz Baso 2019) by transforming the B_x and B_y components of the magnetic field to $B_{p1} = B_t \cos 2\phi$ and $B_{p2} = B_t \sin 2\phi$, where $B_t^2 = B_x^2 + B_y^2 = B_{p1}^2 + B_{p2}^2$ is the square of the transverse component of the magnetic field, and $\phi = \arctan(B_y/B_x)$ is the azimuth. We found this solution to be very stable and provide good results.

The original simulation pixel of 16 km is rebinned to the Hinode spatial sampling of $0.16''$ per pixel, resulting in a pixel

size of 116 km. No previous convolution with the spatial PSF of the telescope is applied to the physical parameters, so that the output of the trained model will be deconvolved (unaffected by the PSF) atmospheric parameters, in fashion similar to Asensio Ramos & Díaz Baso (2019). Horizontal cuts at constant $\log \tau_{500}$ between -4 and 1 in steps of 0.5 are extracted. This results in 11 depth points for each of the physical parameters, so that the total dimension of the parameter space per column is $d = 77$.

The Stokes profiles in the Fe I 6301.5 and 6302.5 Å lines are synthesized at disk center⁴ under the LTE approximation using a parallel version of SIR (Ruiz Cobo & del Toro Iniesta 1992; Asensio Ramos & Díaz Baso 2019). We convolve the emergent Stokes profiles with the measured spatial and spectral point spread functions (PSF) of Hinode/SOT (Tsuneta et al. 2008; Danilovic et al. 2008). The results are resampled to the spectral (21.5 mÅ per pixel) and spatial sampling ($0.16''$ per pixel) of the Hinode/SP instrument. This results in 112 wavelength points for each Stokes parameters. Gaussian noise with a standard deviation of 10^{-3} is added to the profiles, which is a typical value for Hinode/SP observations. We finally point out that the line formation region of the Fe I lines almost never reaches $\log \tau_{500} = -4$. However we included this depth point in the training set and we caution that the information obtained at these heights is purely learned from the statistical correlations present in the training data conditioned on the observed Stokes profiles.

⁴ This is a current limitation of the trained model, which can only analyze observations close to disk center. This can be trivially solved by using other heliocentric angles in the training set.

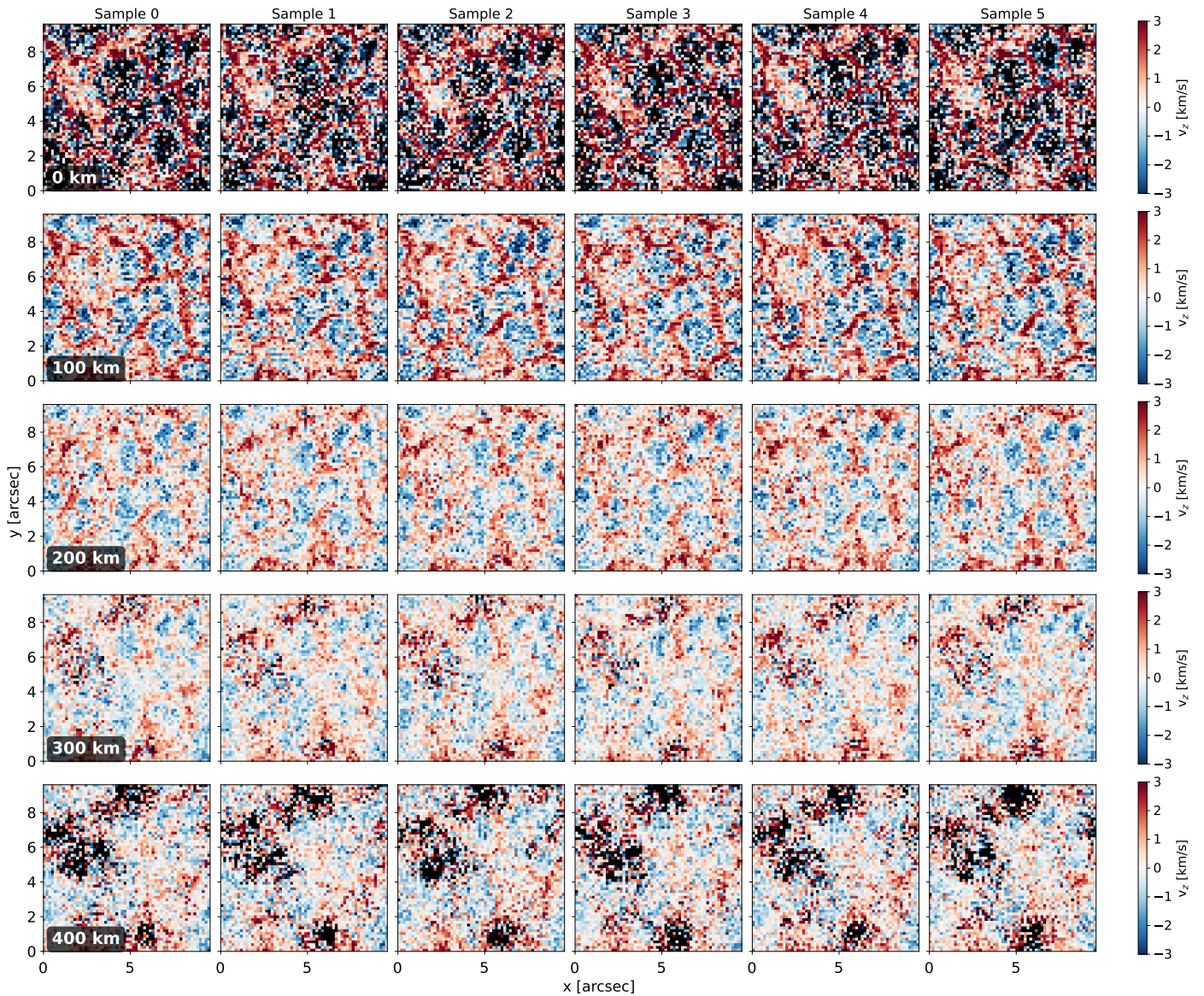


Fig. 2: Five samples from the posterior distribution for the vertical velocity computed with the flow matching generative model conditioned on the observed Stokes profiles.

3.2. Architecture and training details

A total of 10^5 training patches of size 64×64 pixels are extracted from the original snapshots, randomly choosing among the snapshots considered for training. The location of the patches is randomly selected, ensuring that they are fully contained within the original simulation box. Random horizontal and vertical flips, together with random rotations in multiples of 90° are applied to the patches to augment the training data. Each patch is then a tensor $C \times H \times W$, where $C = 77$ is the number of channels corresponding to the physical parameters, and $H = W = 64$ are the height and width of the patch in pixels. The corresponding Stokes profiles are also extracted in patches of the same size, resulting in a tensor of shape $L \times H \times W$, where $L = 448$ is the concatenation of the four Stokes parameters (112 wavelength points each).

The median and standard deviation of the physical parameters are computed for the training dataset and stored. During training, the physical parameters are normalized by subtracting the median and dividing by three times the standard deviation.

The Stokes profiles are also normalized. Stokes I is normalized by dividing by 0.5 and subtracting 0.5. Stokes Q and U are normalized by multiplying by 100, while Stokes V is normalized by multiplying by 10. We have found this normalization to be stable during training, giving good results. We note that the normalization of the Stokes parameters Q , U and V is always problematic, given their large dynamic range.

The Stokes profiles are then processed by a conditioning U-Net (Ronneberger et al. 2015) to extract a latent representation that summarizes the information contained in the Stokes profiles. We choose to use a U-Net architecture for the conditioning model because of its ability to capture multi-scale spatial features, which are relevant for the prediction of the atmospheric parameters. This U-Net takes as input the Stokes profiles as a tensor of shape $L \times H \times W$ and produces a latent representation of shape $Z \times H \times W$. We empirically choose $Z = 64$ as the number of channels in the latent representation, similar to $C = 77$, with the idea of preserving enough information for conditioning for

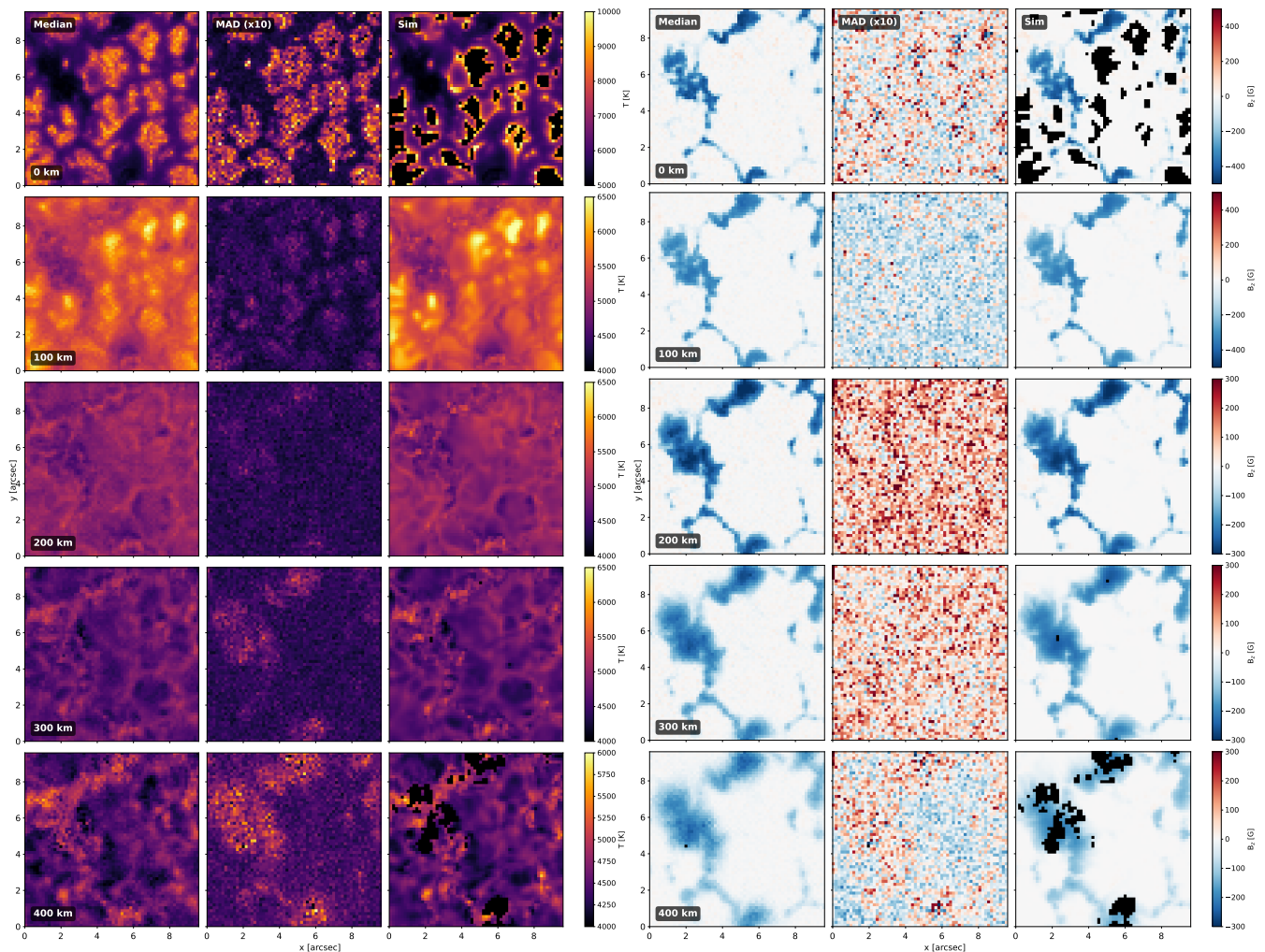


Fig. 3: Inferred height-dependent temperature (left three panels) and vertical magnetic field (right three panels). The true values from the simulation are shown in the third column of each panel, while the median and MAD of the output probability distributions are shown in the first and second columns of each panel. Note that the MAD is multiplied by a factor of 10 so that all panels share the same color bar.

the velocity model. However, this is a hyperparameter that can be surely optimized.

The velocity model $v_t^{\theta}(X_t, S)$ is another U-Net which takes as input a tensor of size $D \times H \times W$, where $D = 77 + 64$ is the number of channels corresponding to the concatenation of the current state X_t and the learned representation of the conditioning Stokes profiles S . The time step t is also embedded using a sinusoidal positional embedding and concatenated with the input of the velocity U-Net.

The conditioning and velocity models are implemented with the PyTorch package, and trained on a single NVIDIA RTX 4090 GPU using half precision numbers. We train for 20 epochs with a batch size of 64 using the Adam optimizer (Kingma & Ba 2015) with an initial learning rate of 3×10^{-4} , which is slowly annealed during training using a cosine law until reaching 9×10^{-5} . The time per epoch is around 5 min for a total training time of around 1.5 hours, which is very fast for a model of this complexity and dimensionality.

4. Validation

4.1. Maps of atmospheric parameters

Once trained, the model is applied to the validation set, the snapshot with mixed polarities that was not used during training. The ODE of Eq. (8) is solved with the learned velocity model to transport 25 samples from the base distribution to the target distribution. This produces 25 samples of the 3D stratification of the atmospheric parameters, evaluated at the fixed optical depth points defined in the training data. The posterior distribution of the atmospheric parameters can be characterized by analyzing the statistics of these samples. Figure 1 shows the vertical stratification with optical depth of three different columns in the FoV, marked with color symbols in the first panel. The first column shows the continuum intensity normalized to the average continuum, together with the total linear polarization and circular polarization in the wing of the line. The thin blue curves in the rest of panels display the median (50th percentile) of the posterior distribution for each optical depth and physical quantity, while the shaded regions corresponds to the area between the 25th and 75th (dark blue) and the 5th and 95th percentiles (light blue). The true values from the simulation are shown in orange.

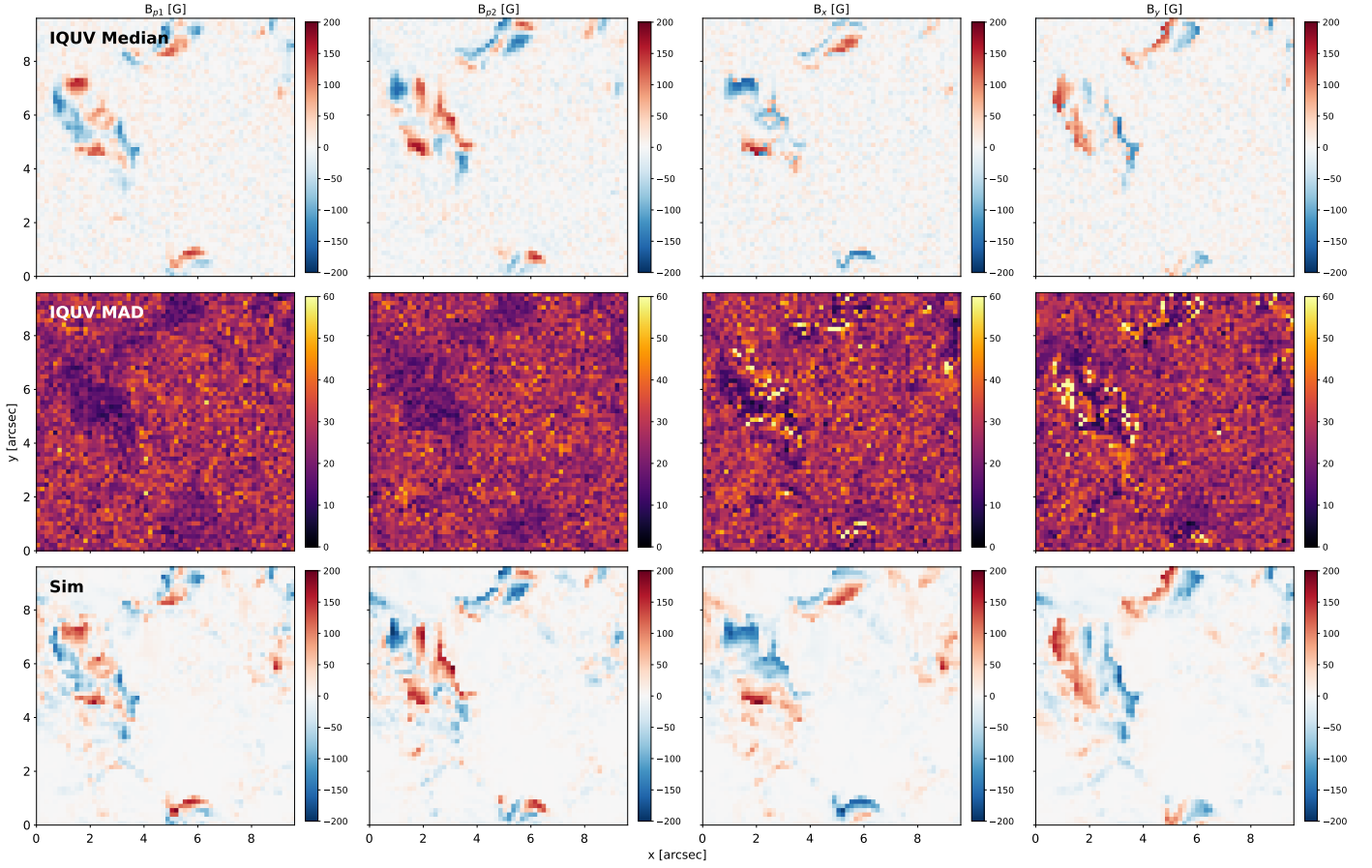


Fig. 4: Inferred ambiguous (left two panels) and disambiguated (right two panels) transverse components of the magnetic field for 100 km above the height at which the average optical depth is unity. The median of the posterior is shown in the first row, the MAD of the posterior is shown in the second row, and the true values from the simulation are shown in the third row.

The results show that the model is able to capture the true values within the considered percentiles of the posterior distribution. Larger uncertainties are found in the lower and upper layers of the atmosphere, which is expected given that the lines are mostly sensitive to the region between $\log \tau_{500} = -2.5$ and $\log \tau_{500} = 0$. The code reliably produces a median value for B_z close to the true value for the most magnetized pixel (blue star), and returns something compatible with zero for the less magnetized regions (orange and green stars).

Given that the model produces an estimation of the height of each optical depth surface, it is possible to use interpolation to obtain the inferred atmospheric parameters as a function of geometrical height (see, e.g., Asensio Ramos & Díaz Baso 2019). Figure 2 shows five different samples from the posterior distribution for the vertical velocity at five different geometrical heights. The changes in optical depth naturally occurring due to changes in the temperature and density, together with the presence of Wilson depressions in the presence of magnetic fields, produce that each column in the FoV has a different mapping between optical depth and geometrical height. This induces that the physical properties of granules very deep in the atmosphere are missing (marked as black regions in the panels at 0 km), while the physical properties of intergranular lanes and magnetic elements are missing in the upper geometrical layers of the atmosphere (marked as black regions in the panels at 400 km). There is a significant amount of variability among the samples, which is a consequence of the Bayesian nature of the simulation-based model. Those regions for which the model uncertainty is smaller vary

less between samples. Note that the mapping between optical depth and geometrical height is also a random variable sampled from the posterior and, as such, different for each sample. Therefore, the interpolation needs to be carried out independently for each sample.

Robust statistical summaries of the posterior distribution can be obtained directly from the samples. Figure 3 shows the inferred median and median absolute deviation (MAD) of the posterior distribution for temperatures and vertical magnetic fields as a function of geometrical height, alongside their true values in the validation snapshot. Because we crop the simulations at $\log \tau_{500} = 1$ and $\log \tau_{500} = -4$, we lack access to the temperature and velocity in certain parts of the Field of View (FoV) at 0 and 400 km for the simulation. Consequently, the third column of each panel features black patches representing these missing data regions⁵. Interestingly, as long as at least one sample from the posterior yields a valid value for a given pixel, both the median and MAD can still be computed. In other words, the Bayesian nature of the model allows us to extract meaningful information about the physical parameters even for regions close to the limits of the line formation region, so that there are fewer missing regions. This information is, however, highly uncertain, as indicated by the increased MAD. Anyway, we checked that

⁵ It is always possible to extract cuts at constant vertical height from the original snapshot that are not affected by the missing regions, a direct consequence of the corrugated constant optical depth surfaces.

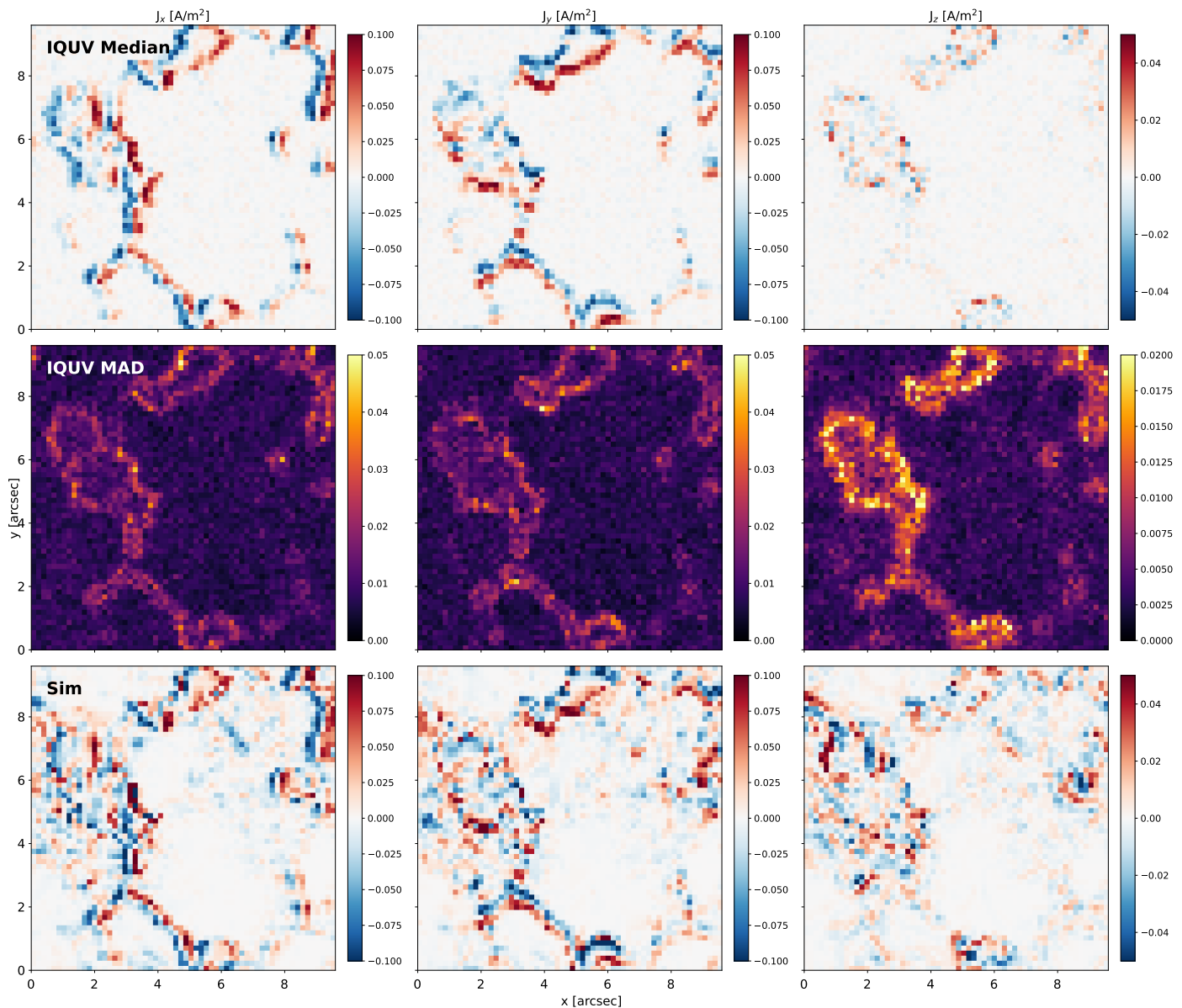


Fig. 5: Divergence of the magnetic field (left) and the three cartesian components of the electric current density (right three panels) obtained after disambiguating the transverse components of the magnetic field at 100 km. The median and MAD of the posterior are shown in the first and second rows, respectively. The last rows shows the inference in the MHD snapshot.

the estimated physical parameters are similar to those of the original snapshot at constant geometrical height.

Overall, the results show that the median model is highly similar to the depth stratification of the physical quantities in the simulation. This is a remarkable finding, demonstrating that the model can reliably learn the relationship between optical depth and geometrical height by leveraging the correlations present in the training data.

4.2. Disambiguation and electric currents

Since our model allows us to infer physical quantities in a geometrical scale as a natural consequence of taking advantage of the inherent statistical correlations present in the training data, it is almost straightforward to disambiguate the transverse components of the magnetic field. Contrary to more standard methods, we do not need to rely on any field extrapolation method (see,

e.g., [Metcalf et al. 2006](#)) or extra assumptions ([Borrero et al. 2021](#)). To this end, we use an in-house version of the minimum energy method developed by [Metcalf \(1994\)](#) and later modified by [Metcalf et al. \(2006\)](#) that is described in Appendix A. This makes it more similar to the method developed by [Yang et al. \(2025\)](#), which starts from an inverted stratified ambiguous field and is only based on the divergence-free nature of the magnetic field.

Figure 4 displays the posterior median in the upper panel, the MAD in the middle panel, and the true values from the simulation in the lower panel for the ambiguous and disambiguated transverse components of the magnetic field. Although we can compute the criterion for the disambiguation at different heights, we choose to carry out the disambiguation at a fixed height of 100 km for visualization purposes. The results demonstrate that computation of the vertical derivatives using the inferred height dependence is very precise, producing disambiguated transverse

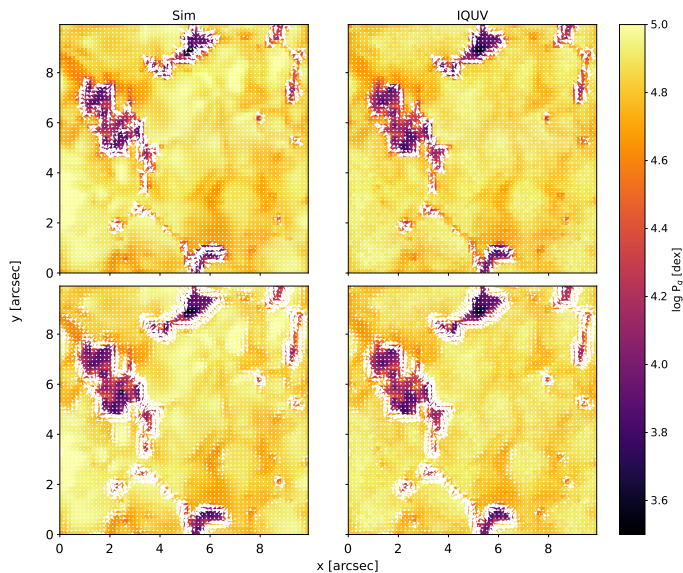


Fig. 6: Logarithm of the gas pressure (background image), Lorentz force (arrows in the upper panels) and gas pressure gradient (arrows in the lower panels).

components of the magnetic field that are strikingly similar to the true values from the simulation. The posterior MAD for the more magnetized regions for B_{p1} and B_{p2} is smaller than in the rest of the FoV, a consequence of the larger Stokes Q and U signals in those regions. The uncertainty in the disambiguated transverse components of the magnetic field is, in general, larger than in the ambiguous components, which is specially relevant in the borders of the magnetized regions, where some patches show the wrong polarity. However, all in all, the inferred model can be used to correctly disambiguate the more magnetized regions of the quiet Sun, producing a solution with very low divergence and electric currents.

Having access to the disambiguated magnetic field allows us to calculate electric current density maps. Electric currents are relevant for the energy balance of the solar atmosphere, since they can be dissipated by Ohmic and ambipolar diffusion (Priest 1999; Komenko & Collados 2012). As such, they can be considered as proxies of highly non-potential magnetic fields, which can produce explosive events in higher layers of the atmosphere. Since \mathbf{J} depends on horizontal and vertical gradients of the magnetic fields, they are often obtained from observations using magnetic field extrapolation methods or a-posteriori treatment of standard inversion methods (Puschmann et al. 2010a,b). However, some recent efforts (Pastor Yabar et al. 2021) have opened up the possibility of obtaining \mathbf{J} from observations by resorting to the use of magnetohydrostatic equilibrium (MHS). These results make use of a newly developed Stokes inversion code developed by Borrero et al. (2021), where the MHS condition is imposed as a regularization during the inversion process. The method allows to obtain the electric current density in the photosphere with sufficient precision, according to Borrero & Pastor Yabar (2023). More recently, Yang et al. (2025) demonstrated a new promising strategy that is based on using physics-informed neural networks to infer \mathbf{J} .

Contrary to previous approaches, in this work we can obtain \mathbf{J} directly from the inferred magnetic field without any additional assumption, apart from those encoded in the generative model. The resulting maps are displayed in Fig. 5, with a direct comparison to the true values obtained from the MHD snap-

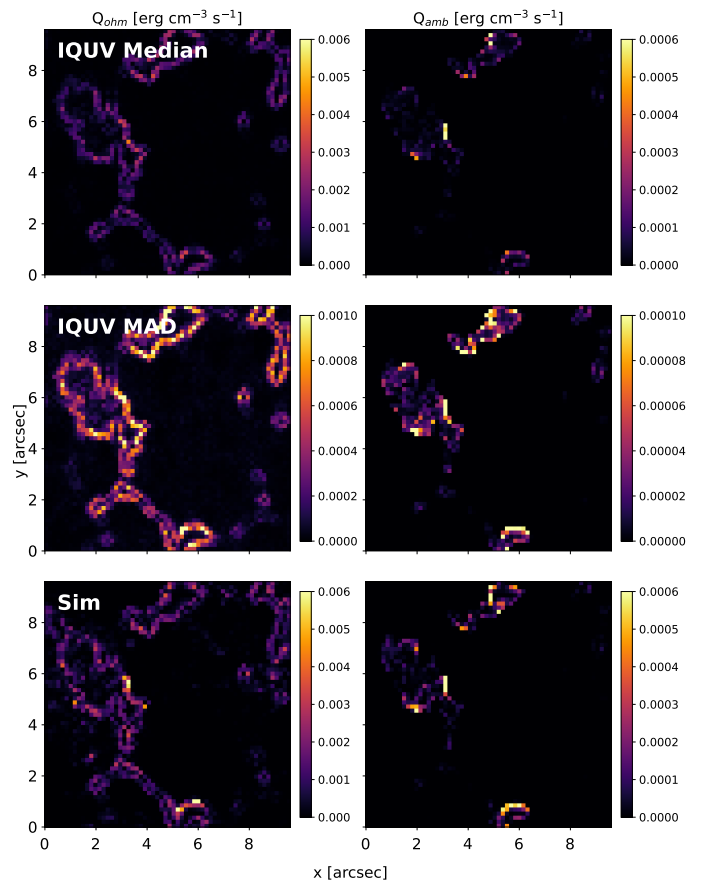


Fig. 7: Ohmic (left) and ambipolar (right) dissipation maps for the validation set.

shot. There is a remarkable similarity between the median value and the value of \mathbf{J} calculated from the true values of the simulation, despite the increased uncertainty. It is worth noting that the value for \mathbf{J} outside of clearly magnetized regions is compatible with zero, with an uncertainty as low as $0.0025\text{-}0.0050 \text{ A m}^{-2}$. In this sense, our result compares very favorably with those of Borrero & Pastor Yabar (2023), who find a value of 0.05 A m^{-2} for the regions where no polarimetric signal is detected.

4.3. Lorentz force

The Lorentz force $\mathbf{F}_L = \mathbf{J} \times \mathbf{B}$ can be computed from the inferred electric current density and magnetic field. We can then compare its value with the inferred gas pressure gradient ∇P to check the consistency of the MHS equilibrium. Figure 6 shows maps of the gas pressure at a geometrical height of 100 km as a background, both for the simulation (left panels) and the median value from the posterior distribution (right panels). The arrows in the upper panels show the horizontal components of the Lorentz force, computed from \mathbf{J} and \mathbf{B} , while those in the lower panels show the horizontal components of the gas pressure gradient, computed using finite differences. Their similarity is remarkable.

4.4. Dissipation

Finally, we can compute the Ohmic and ambipolar dissipation maps at any arbitrary height (note that the Hall dissipation is zero). They can be computed using (see, e.g.,

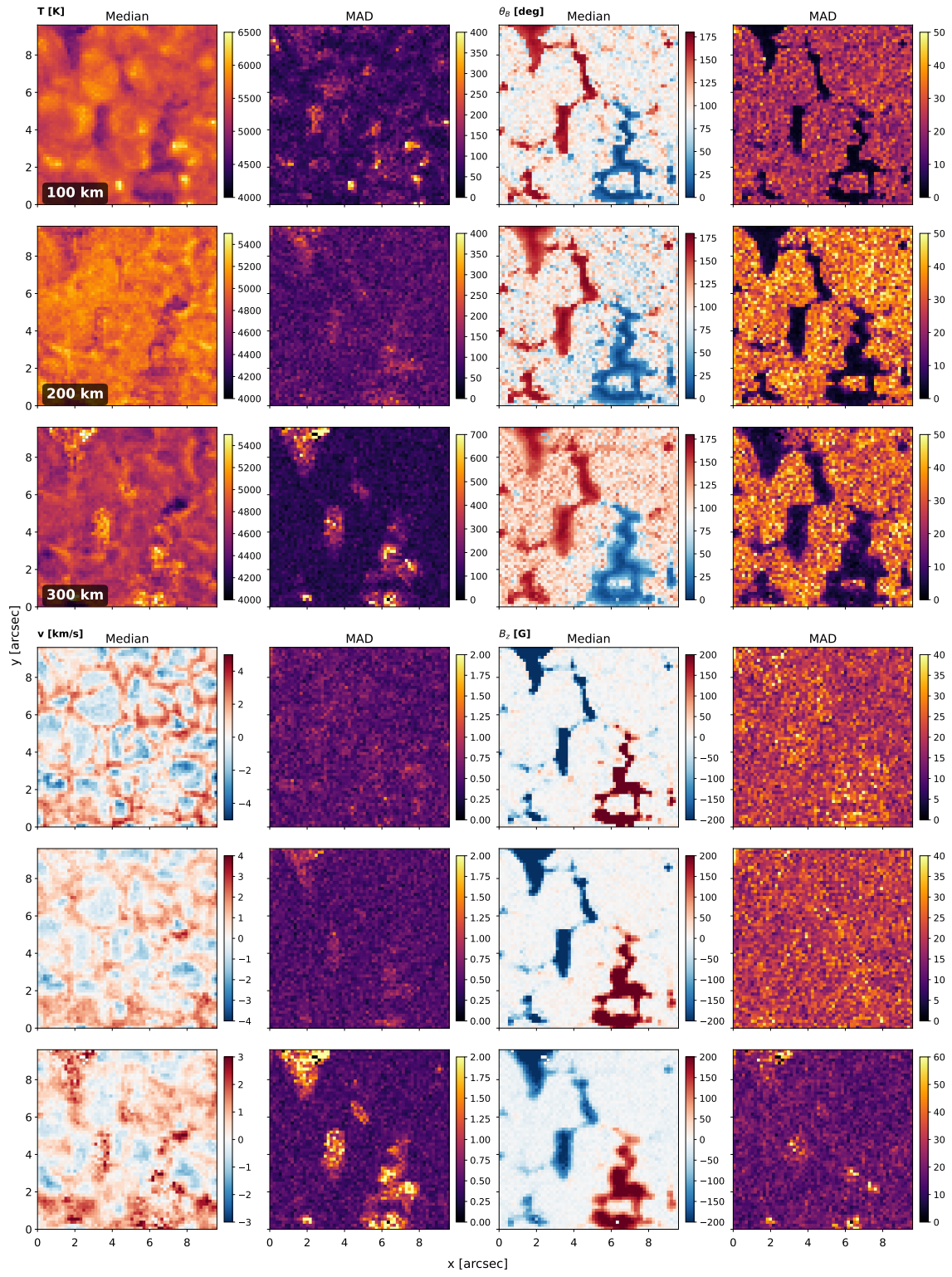


Fig. 8: Inferred height-dependent temperature, line-of-sight velocity, inclination angle the magnetic field and line-of-sight component of the magnetic field for the quiet Sun Hinode/SP scan. Each variable is shown at three different constant geometrical heights, with the two columns showing the median and the MAD of the distribution, respectively.

(Khomenko & Collados 2012):

where

$$\eta = \frac{m_e (v_{ei} + v_{en})}{e^2 n_e} \quad (10)$$

$$Q_{\text{Ohm}} = \eta J^2, \quad Q_{\text{amb}} = \eta_A |\mathbf{J} \times \mathbf{B}|^2, \quad (9)$$

$$\eta_A = \frac{(\rho_n / \rho)^2}{\rho_i v_{in} + \rho_e v_{en}} \quad (11)$$

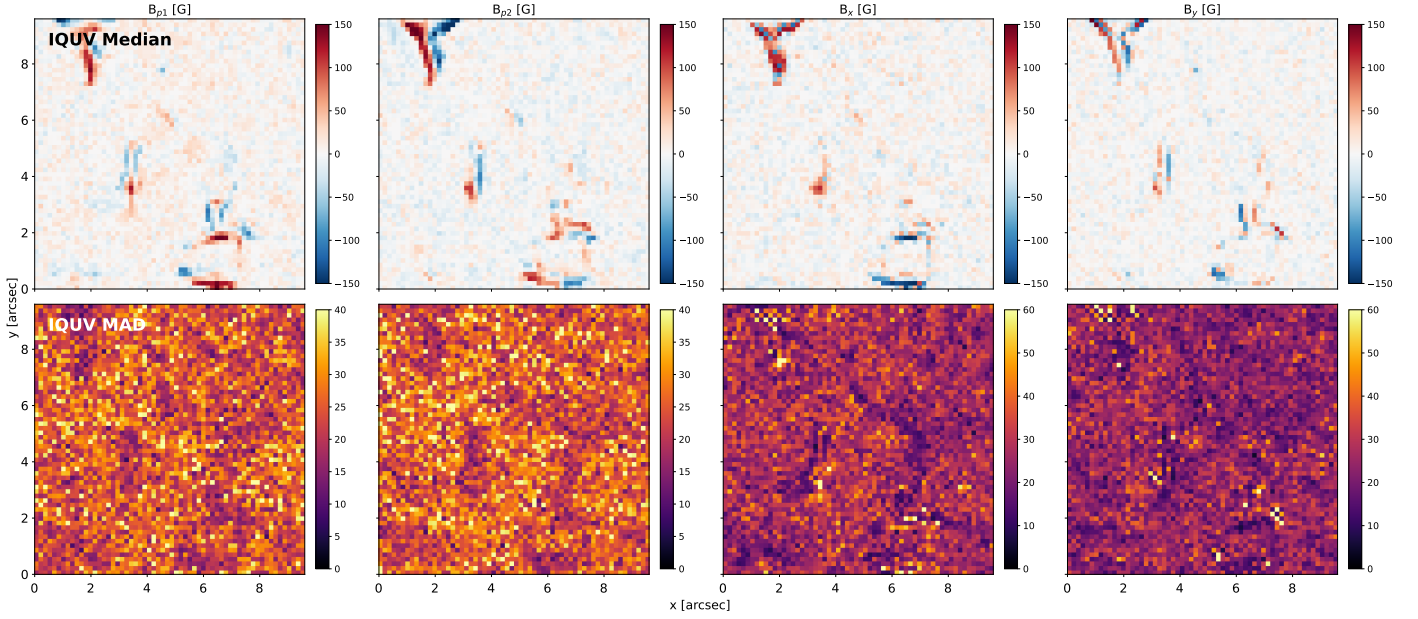


Fig. 9: Inferred ambiguous (left two panels) and disambiguated (right two panels) transverse magnetic fields. The upper panels display the median of the posterior distribution, while the lower panels show the MAD.

are the Ohmic and ambipolar diffusivities, respectively. They depend on the collision frequencies between electrons, ions and neutrals, which are calculated using the formulas provided by [Khomenko & Collados \(2012\)](#):

$$\begin{aligned} v_{in} &= n_n \sqrt{\frac{8k_B T}{\pi m_{in}}} \sigma_{in} \\ v_{en} &= n_n \sqrt{\frac{8k_B T}{\pi m_{en}}} \sigma_{en} \\ v_{ei} &= \frac{4}{3} \sqrt{\frac{2\pi}{m_e}} \frac{n_e e^4 \Lambda}{(k_B T)^{3/2}}. \end{aligned} \quad (12)$$

The cross sections take the values $\sigma_{in} = 5 \times 10^{-15} \text{ cm}^2$ and $\sigma_{en} = 10^{-15} \text{ cm}^2$, the Coulomb logarithm is calculated as $\Lambda = 23.4 - 1.15 \log_{10} n_e + 3.45 \log_{10} T$, where n_e is measured in cm^{-3} and T in eV and m_{in} and m_{en} are the reduced masses of the ion-neutral and electron-neutral collisions, respectively. The density of neutrals and electrons is computed by applying the LTE equation of state used in SIR to the inferred temperature and gas pressure, while that of ions is obtained by applying the charge neutrality condition, so that $\rho_i = \rho_e$.

The resulting maps of Q_{Ohm} and Q_{amb} are shown in Fig. 7, where we can see that the Ohmic dissipation is mostly localized in the borders of the magnetized regions, while the ambipolar dissipation is less extended and is only significant where there is a measurable transverse component of the magnetic field. The inferred values of the dissipation are perfectly compatible with those obtained from the true values of the simulation. Uncertainties are larger in the borders of the magnetized regions, but their amplitude are small, becoming only slightly larger than 10%.

5. Quiet Sun Hinode observations

Having checked the performance of the model on synthetic data, we apply it to real observations. We use the Hinode/SP scan of a quiet Sun region at disk center taken on 2007-03-10 at 11:37 UT and analyzed in [Lites et al. \(2008\)](#). The scan consists of a

1024×2048 pixels with a spatial sampling of 0.16" per pixel, of which we extract a tiny subfield of 64×64 pixels that contains magnetic elements of the two polarities. The Stokes profiles are normalized in the same way as the training data, and then fed into the conditioning U-Net to extract the latent representation. The flow matching model then produces 25 samples of the posterior distribution.

The resulting maps at constant geometrical height for T , v , B_z , and θ_B are shown in Fig. 8, where we show the median and the MAD of the posterior distribution. Given that the flow matching model produces samples from the posterior, derived quantities like θ_B are trivially obtained by calculating the derived quantity for each sample and then calculating the statistics of the resulting distribution. The results show that the magnetized regions contain vertical magnetic fields of both polarities at the core of the magnetic elements, with a strong horizontal gradient towards essentially undetectable magnetic fields in the granular regions. The uncertainty of the model on the inclination of the field in the magnetized regions is almost negligible. We also witness the canopy structure of the magnetic field, with broader structures at 300 km than at 100 km.

Motivated by the encouraging results obtained in the validation set concerning the estimation of \mathbf{J} , we apply the minimum energy method to disambiguate the transverse components of the magnetic field to compute such current densities. The disambiguated transverse components are shown in Fig. 9, where we show the ambiguous and disambiguated transverse components of the magnetic field, together with their MAD. Except for some very localized patches in which the MAD is sizable, the results seem to indicate a very clear disambiguated solution. The majority of the FoV is compatible with zero transverse magnetic field, which is expected in the quiet Sun, given that the Stokes Q and U signals are very weak. Despite that the only patches with significant transverse magnetic field are those corresponding to the strongest magnetic elements displayed in Fig. 8, the inferred \mathbf{J} , shown in Fig. 10, is very well localized. Strong currents appear, with both signs, in the borders of the magnetized regions. The posterior uncertainty is sufficiently low to ensure that the

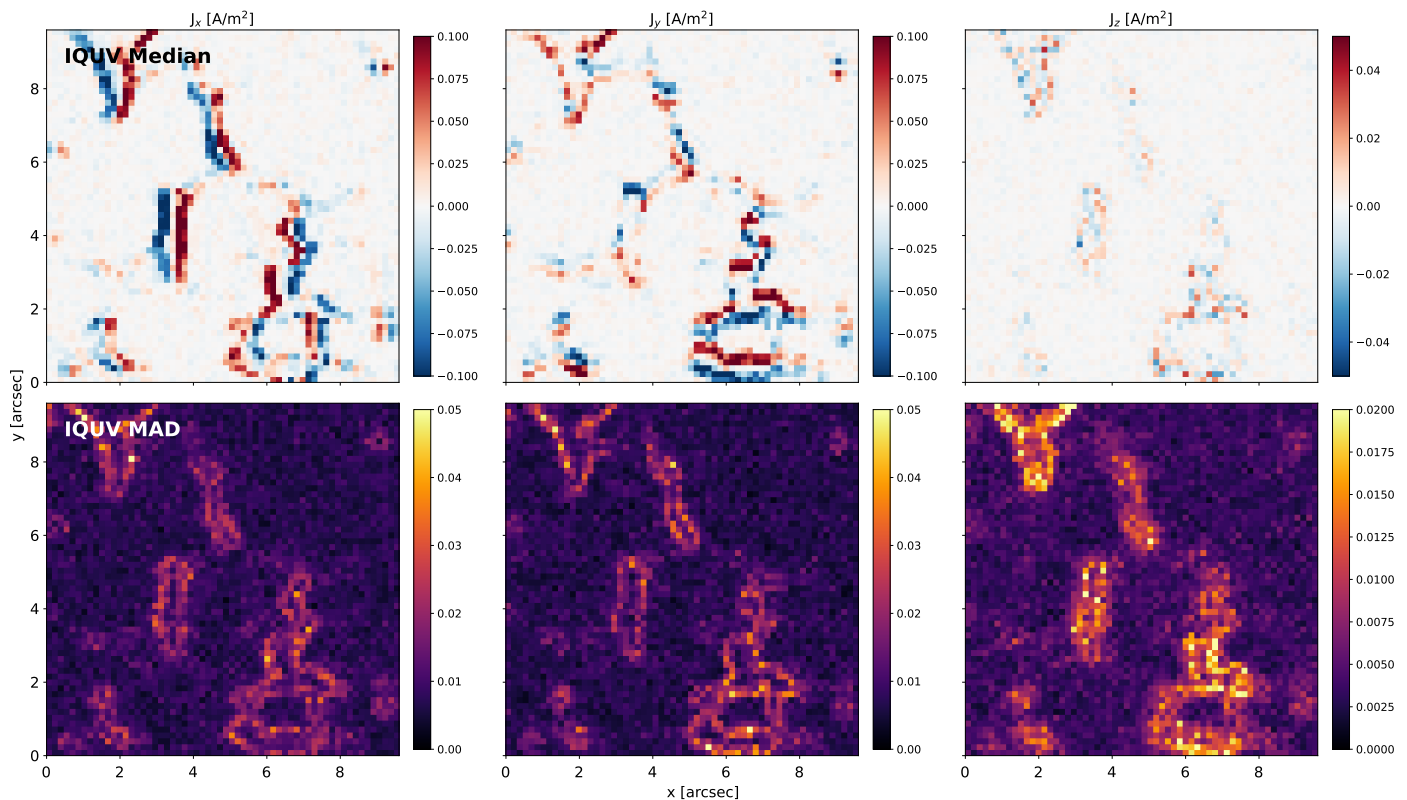


Fig. 10: Inferred electric current density maps for the Hinode/SP quiet Sun observation of Fig. 8.

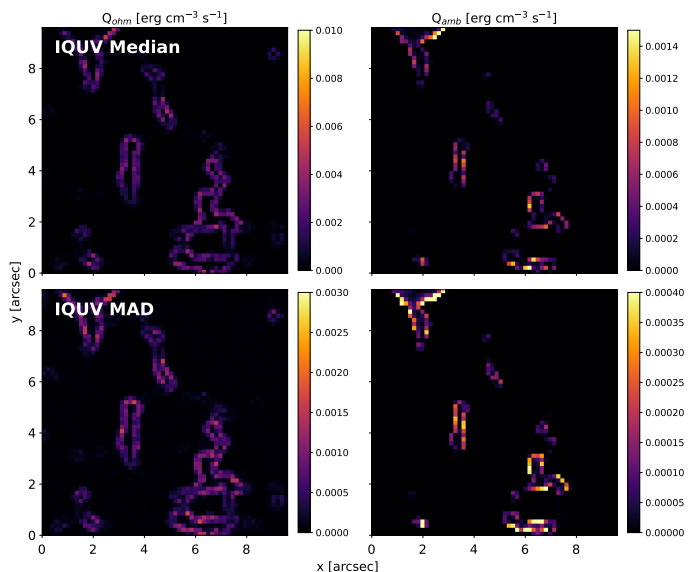


Fig. 11: Ohmic (left) and ambipolar (right) dissipation maps for the Hinode/SP quiet Sun observation of Fig. 8.

measured currents are real and not a consequence of the noise in the data.

Equipped with the inferred \mathbf{B} and \mathbf{J} , we can calculate the Ohmic and ambipolar dissipation maps, which are shown in Fig. 11. The results show that the both types of dissipation are compatible with zero in the regions where we do not detect any magnetic field. Again, Ohmic dissipation is mostly localized in the borders of the magnetized regions, while the ambipolar dissipation is more important in regions with a measurable transverse

component of the magnetic field, and much less spatially extended. Ambipolar dissipation is also smaller in absolute value than Ohmic dissipation. This is expected in the photosphere, where the plasma is mostly neutral and the magnetic field is not strong enough to strongly decouple neutrals and ions.

6. Small-scale loop emergence

As a final application, we show a preliminary analysis of the Hinode/SP scans of one of the small-scale loop emergence events analyzed by [Martínez González & Bellot Rubio \(2009\)](#). A more detailed analysis will be presented in a future study.

Small-scale magnetic loops were identified as two opposite-polarity circular polarization signals flanking a linear polarization signal ([Martínez González et al. 2007](#); [Centeno et al. 2007](#)). Their temporal coherence strongly suggested that they corresponded to organized, connected magnetic field structures in the form of Ω - or U-loops. Their three-dimensional geometry was previously inferred by [Ishikawa et al. \(2010\)](#) and [Martínez González et al. \(2010\)](#) through pixel-by-pixel inversions in the optical depth scale and in a non-consistent geometrical height, respectively. Here, we reconstruct the three-dimensional geometry in a consistent geometrical height scale and analyze the temporal evolution of the transverse and longitudinal components of the magnetic field as a function of geometrical height.

In Figure 12, a three-dimensional magnetic structure in the form of a loop ascending through the photosphere can be clearly identified. During the first two snapshots, only the transverse magnetic field is visible, corresponding to the apex of the loop. This predominantly horizontal structure exhibits an approximate vertical extent of 200 km, with the transverse field reaching its maximum intensity around that height.

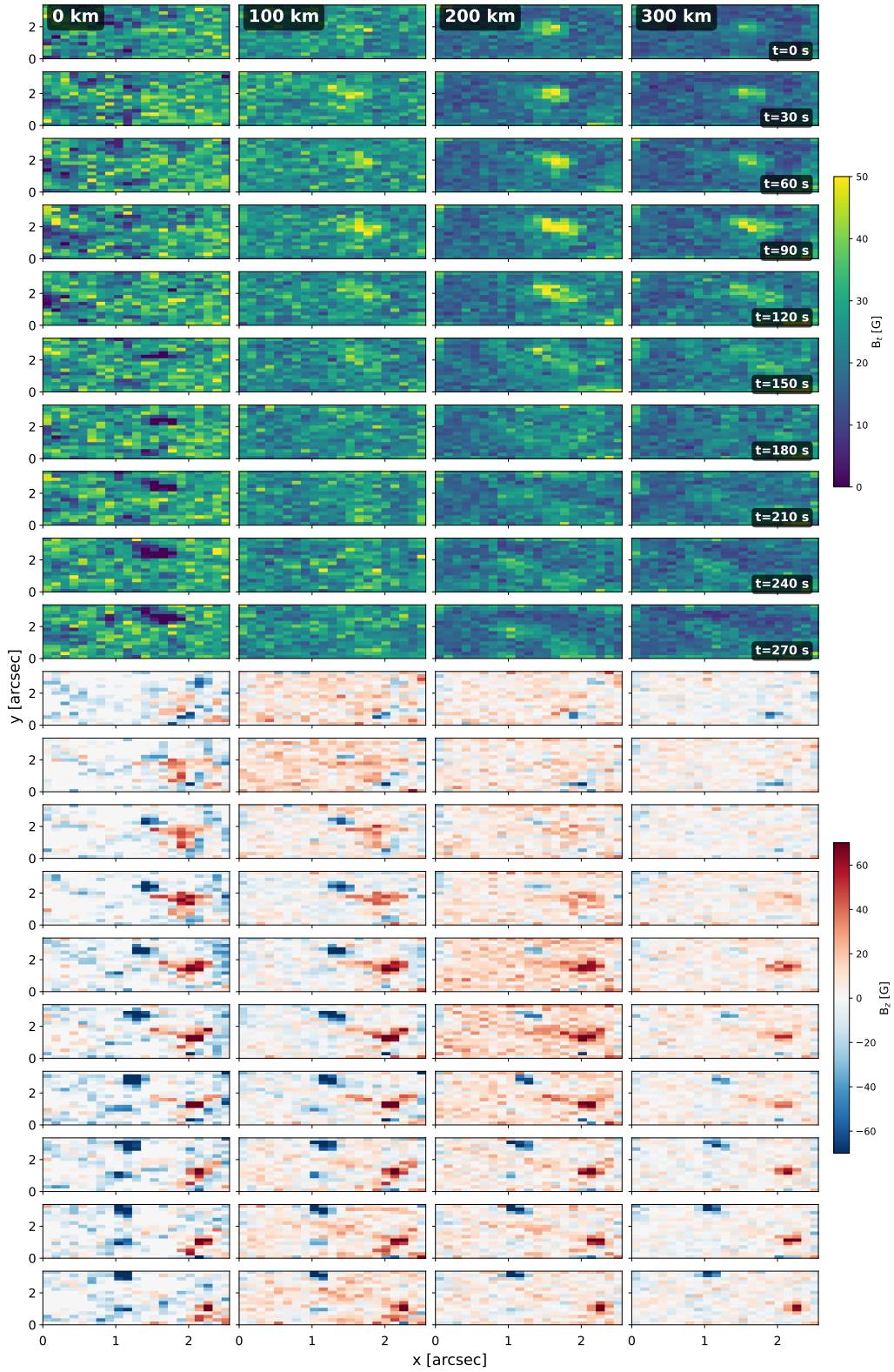


Fig. 12: Transverse (upper panels) and longitudinal (lower panels) components of the magnetic field for the emerging small-scale loop.

At $t=60$ s, opposite-polarity regions appear at both ends of the transverse field, extending from 0 to 100 km. These regions correspond to the loop footpoints connecting to the apex. At a height of 200 km, the same polarity pattern and a slight inclination of the footpoints, reflected in a weaker longitudinal field component, are observed, supporting the interpretation of a sin-

gle connected magnetic structure. At $t=90$ s, the footpoints become visible up to 300 km, while the linear polarization signal is strongest at the highest layers. This behavior indicates that the loop continues to rise through the photosphere.

At $t=120$ s, the transverse field weakens and the longitudinal field at the footpoints becomes stronger at all heights. This sup-

ports the hypothesis of an ascending loop, since the upper part of the loop is already leaving the line formation region and the more vertical part of the loop is penetrating this region. At this stage, the loop reaches a height of approximately 300 km and a horizontal extent of about 700 km, resulting in a very flattened loop. This is consistent with the results of [Martínez González et al. \(2010\)](#), who, for $t=120$ s, reported a loop height of 300 km and a horizontal extent of about 750 km (see their Figure 1). Finally, the apex of the loop leaves the formation region at $t=150$ s, and only the footpoints remain visible as they continue to separate with time.

7. Conclusions and future work

We have presented 3DStokesFlow, a new code for the inversion of Stokes profiles based on conditional flow matching. The code has been trained with the quiet Sun simulations of the SPIN4D project, for the pair of lines at 630 nm and for disk center observations. It has been validated with a snapshot with mixed polarities that was not used during training. The results show that the model is able to capture the true values of the atmospheric parameters, providing samples from the posterior distribution, which allows us to characterize the uncertainty and correlation of the inferred parameters. The model is able to return the physical parameters as a function of geometrical depth, which allows us to disambiguate the transverse components of the magnetic field without any field extrapolation method. This opens up the possibility of calculating electric current density maps and dissipation with high precision.

The application to Hinode/SP quiet Sun observations shows that the model can be safely applied to real data. We have produced, for the first time, reliable (with uncertainties associated) maps of the electric current density and Ohmic and ambipolar dissipation in the quiet Sun. Additionally, we find unequivocal evidence of the loop-like structure in geometrical height of the magnetic field.

We are perfectly aware of the limitations of this code and we have long-term ideas to address them. First, the results are dependent on the availability and realism of MHD simulations. For this reason, only quiet Sun simulations in the photosphere have been used for training, where the state-of-the-art MHD simulations are considered to be sufficiently realistic. For this reason, the model is expected to perform well only in quiet Sun regions in the photosphere. More active regions and higher layers of the atmosphere are not included in the training data because of the lack of consensus on how realistic these MHD simulations are. The model can be trivially extended to those regions once such simulations are available.

Second, the model has been trained with disk center observations at the pair of Fe I lines at 630 nm. Extending it to other lines of sight is straightforward, although we would need to add a conditional variable to the model to encode the angle of observation. Additionally, alternative encoders of the Stokes profiles (e.g., based on the transformer architecture) could be used to make the model more flexible and able to deal with different spectral lines.

Third, we have limited the training to the relatively reduced spatial resolution provided by the Hinode/SP instrument. On one hand, this allows the model to be applied to the enormous amount of Hinode/SP data available in the archives. On the other hand, it limits the performance of the model for more modern telescopes, such as the Daniel K. Inouye Solar Telescope (DKIST; [Rimmele et al. 2020](#)) and the future European Solar Telescope (EST; [Quintero Noda et al. 2022](#)). The extension to

higher spatial resolution is feasible but not straightforward. From a computational point of view, the transfer and storage of MHD simulations at a resolution of 28 km (the DKIST diffraction limit at 630 nm) for training is difficult. On the other hand, training generative models directly in pixel space at such high resolution is probably not feasible. For this reason, we speculate that the extension to higher spatial resolution will require the use of a generative flow matching model in a latent representation. Following [Rombach et al. \(2022\)](#), this latent representation can be obtained by pre-training a variational autoencoder (VAE) on the MHD simulations, and then training the flow matching model in the latent space of the VAE.

Additionally, in the present implementation, the azimuthal disambiguation is performed as a separate post-processing step. Since the adopted algorithm makes use of information from neighbouring pixels, it is possible to incorporate the disambiguation directly into the Stokes inversion through a spatially coupled convolutional neural network-based framework. This extension is currently in preparation ([Glaser et al. 2026](#)).

Finally, the current version of the code is not providing any information about the transverse velocity components, which are relevant for the energy balance of the solar atmosphere. Although they can be easily estimated from time series of observations ([Asensio Ramos et al. 2017](#)), we want to explore whether it is possible to infer them by exploiting the correlation between the velocity and magnetic field in the training data.

Acknowledgements. We acknowledge the critical read of an early draft provided by J. de la Cruz Rodríguez. A.A.R. acknowledges funding from the Agencia Estatal de Investigación del Ministerio de Ciencia, Innovación y Universidades (MCIU/AEI) under grant “Polarimetric Inference of Magnetic Fields” and the European Regional Development Fund (ERDF) with reference PID2022-136563NB-I00/10.13039/501100011033. K.Y., S.C.D. and X.S. are supported by award 2008334 from the US National Science Foundation. This research has made use of NASA’s Astrophysics Data System Bibliographic Services. The code is publicly available at <http://github.com/aasensio/3DStokesFlow>. We acknowledge the community effort devoted to the development of the following open-source packages that were used in this work: numpy (numpy.org), Harris et al. 2020), matplotlib (matplotlib.org, [Hunter 2007](#)), PyTorch (pytorch.org, [Paszke et al. 2019](#)), scipy (scipy.org, [Virtanen et al. 2020](#)) and scikit-learn (scikit-learn.org, [Pedregosa et al. 2011](#)).

References

- Ardizzone, L., Kruse, J., Wirkert, S., et al. 2018, arXiv e-prints, arXiv:1808.04730
- Asensio Ramos, A. & de la Cruz Rodríguez, J. 2025, A&A, 703, A55
- Asensio Ramos, A. & Díaz Baso, C. J. 2019, A&A, 626, A102
- Asensio Ramos, A., Martínez González, M. J., & Rubiño-Martín, J. A. 2007, A&A, 476, 959
- Asensio Ramos, A., Requerey, I. S., & Vitas, N. 2017, A&A, 604, A11
- Auer, L. H., Heasley, J. N., & House, L. L. 1977, Sol. Phys., 55, 47
- Borrero, J. M. & Pastor Yabar, A. 2023, A&A, 669, A122
- Borrero, J. M., Pastor Yabar, A., & Ruiz Cobo, B. 2021, A&A, 647, A190
- Borrero, J. M., Tomczyk, S., Kubo, M., et al. 2011, Sol. Phys., 273, 267
- Centeno, R., Socas-Navarro, H., Lites, B., et al. 2007, ApJ, 666, L137
- Danilovic, S., Gandorfer, A., Lagg, A., et al. 2008, A&A, 484, L17
- de la Cruz Rodríguez, J. 2019, A&A, 631, A153
- de la Cruz Rodríguez, J., Leenaarts, J., Danilovic, S., & Uitenbroek, H. 2019, A&A, 623, A74
- de la Cruz Rodríguez, J. & van Noort, M. 2017, Space Sci. Rev., 210, 109
- del Toro Iniesta, J. C. & Ruiz Cobo, B. 2016, Living Reviews in Solar Physics, 13, 4
- Díaz Baso, C. J., Asensio Ramos, A., & de la Cruz Rodríguez, J. 2022, A&A, 659, A165
- Frutiger, C., Solanki, S. K., Fligge, M., & Bruls, J. H. M. J. 2000, A&A, 358, 1109
- Glaser, Y., Sadowski, P., Yang, K., et al. 2026, in preparation
- Harris, C. R., Millman, K. J., van der Walt, S. J., et al. 2020, Nature, 585, 357–362
- Hunter, J. D. 2007, Computing in Science Engineering, 9, 90

- Ishikawa, R., Tsuneta, S., & Jurčák, J. 2010, *ApJ*, 713, 1310
- Khomenko, E. & Collados, M. 2012, *ApJ*, 747, 87
- Kingma, D. P. & Ba, J. 2015, in *ICLR (Poster)*, ed. Y. Bengio & Y. LeCun
- Landi Degl'Innocenti, E. & Landolfi, M., eds. 2004, *Astrophysics and Space Science Library*, Vol. 307, *Polarization in Spectral Lines*
- Li, H., del Pino Alemán, T., Trujillo Bueno, J., & Casini, R. 2022, *ApJ*, 933, 145
- Lipman, Y., Havasi, M., Holderrieth, P., et al. 2024, *CoRR*, abs/2412.06264
- Lites, B., Casini, R., Garcia, J., & Socas-Navarro, H. 2007, *Mem. Soc. Astron. Italiana*, 78, 148
- Lites, B. W., Kubo, M., Socas-Navarro, H., et al. 2008, *ApJ*, 672, 1237
- Martínez González, M. J. & Bellot Rubio, L. R. 2009, *ApJ*, 700, 1391
- Martínez González, M. J., Collados, M., Ruiz Cobo, B., & Solanki, S. K. 2007, *A&A*, 469, L39
- Martínez González, M. J., Manso Sainz, R., Asensio Ramos, A., & Bellot Rubio, L. R. 2010, *ApJ*, 714, L94
- Metcalfe, T. R. 1994, *Sol. Phys.*, 155, 235
- Metcalfe, T. R., Leka, K. D., Barnes, G., et al. 2006, *Sol. Phys.*, 237, 267
- Milić, I. & van Noort, M. 2018, *A&A*, 617, A24
- Mistryukova, L., Plotnikov, A., Khizhik, A., et al. 2023, *Sol. Phys.*, 298, 98
- Orozco Suárez, D. & Del Toro Iniesta, J. C. 2007, *A&A*, 462, 1137
- Osborne, C. M. J., Armstrong, J. A., & Fletcher, L. 2019, *ApJ*, 873, 128
- Pastor Yabar, A., Borrero, J. M., Quintero Noda, C., & Ruiz Cobo, B. 2021, *A&A*, 656, L20
- Pastor Yabar, A., Borrero, J. M., & Ruiz Cobo, B. 2019, *A&A*, 629, A24
- Paszke, A., Gross, S., Massa, F., et al. 2019, in *Advances in Neural Information Processing Systems 32*, ed. H. Wallach, H. Larochelle, A. Beygelzimer, F. d'Éric, E. Fox, & R. Garnett (Curran Associates, Inc.), 8024–8035
- Pedregosa, F., Varoquaux, G., Gramfort, A., et al. 2011, *Journal of Machine Learning Research*, 12, 2825
- Priest, E. R. 1999, *Ap&SS*, 264, 77
- Puschmann, K. G., Ruiz Cobo, B., & Martínez Pillet, V. 2010a, *ApJ*, 720, 1417
- Puschmann, K. G., Ruiz Cobo, B., & Martínez Pillet, V. 2010b, *ApJ*, 721, L58
- Quintero Noda, C., Schlichenmaier, R., Bellot Rubio, L. R., et al. 2022, *A&A*, 666, A21
- Rempel, M. 2012, *ApJ*, 750, 62
- Rempel, M. 2014, *ApJ*, 789, 132
- Rempel, M., Schüssler, M., & Knölker, M. 2009, *ApJ*, 691, 640
- Rimmele, T. R., Warner, M., Keil, S. L., et al. 2020, *Sol. Phys.*, 295, 172
- Rombach, R., Blattmann, A., Lorenz, D., Esser, P., & Ommer, B. 2022, in *Proceedings of the IEEE/CVF Conference on Computer Vision and Pattern Recognition*, 10684–10695
- Ronneberger, O., Fischer, P., & Brox, T. 2015, *CoRR*, abs/1505.04597
- Ruiz Cobo, B. & del Toro Iniesta, J. C. 1992, *ApJ*, 398, 375
- Ruiz Cobo, B., Quintero Noda, C., Gafeira, R., et al. 2022, *A&A*, 660, A37
- Socas-Navarro, H., de la Cruz Rodríguez, J., Asensio Ramos, A., Trujillo Bueno, J., & Ruiz Cobo, B. 2015, *A&A*, 577, A7
- Tsuneta, S., Ichimoto, K., Katsukawa, Y., et al. 2008, *Sol. Phys.*, 249, 167
- van Noort, M. 2012, *A&A*, 548, A5
- Virtanen, P., Gommers, R., Oliphant, T. E., et al. 2020, *Nature Methods*, 17, 261
- Vögler, A., Shelyag, S., Schüssler, M., et al. 2005, *A&A*, 429, 335
- Xu, C., Wang, J., Li, H., et al. 2024, *ApJ*, 977, 101
- Yang, K. E., Sun, X., Tarr, L. A., et al. 2025, *ApJ*, 995, 146
- Yang, K. E., Tarr, L. A., Rempel, M., et al. 2024, *ApJ*, 976, 204
- Yang, K. E., Tarr, L. A., Rempel, M., et al. 2024, *The Astrophysical Journal*, 976, 204

Appendix A: Disambiguation of the transverse magnetic field

The disambiguation of the transverse components of the magnetic field is a crucial step in the inference of the magnetic field vector, since the Zeeman effect only provides information about the azimuth of the magnetic field modulo 180° . We have developed a smooth version of the minimum energy method of [Metcalf \(1994\)](#). We make use of the inferred B_{p1} and B_{p2} to compute the still ambiguous solution of B_x and B_y whose azimuth lines in the range $[0, \pi]$. The azimuth is computed as follows:

$$\phi' = \frac{1}{2} \arctan \frac{B_{p2}}{B_{p1}} \pmod{\pi}, \quad (\text{A.1})$$

which can be used to calculate the transverse component of the magnetic field as $B_x = S B_t \cos \phi'$ and $B_y = S B_t \sin \phi'$, where $S = \pm 1$ is the switch that determines the solution of the ambiguity. Strictly speaking, the disambiguation process is a combinatorial problem, since S at each pixel has two possible solutions, resulting in the two options (B_x, B_y) and $(-B_x, -B_y)$. However, the problem can be relaxed to a continuous optimization, which can be solved efficiently with gradient-based methods. This is achieved by defining the per-pixel variable θ and using $S = \tanh \theta$ as a soft switch between the two possible solutions. The variable θ is then optimized by minimizing the following criterion:

$$E = \sum_i (|\nabla \cdot \mathbf{B}| + \lambda |J|)^2, \quad (\text{A.2})$$

where the summation of the criterion is carried out over all pixels in the FoV. The parameter λ is a hyperparameter that controls the relative importance of the two terms in the criterion, which we choose $\lambda = 1$. We again use the Adam optimizer with a learning rate of 10^{-2} to optimize the variable θ for 5000 iterations. After several random initializations, we find that the final solution is very robust and almost insensitive to the initial conditions.

During the optimization, the magnetic field divergence and the cartesian components of the electric current density \mathbf{J} , given in A m^{-2} , are calculated using Ampere's law as:

$$\nabla \cdot \mathbf{B} = \frac{\partial B_x}{\partial x} + \frac{\partial B_y}{\partial y} + \frac{\partial B_z}{\partial z} \quad (\text{A.3})$$

$$J_x = \mu_0^{-1} \left(\frac{\partial B_z}{\partial y} - \frac{\partial B_y}{\partial z} \right)$$

$$J_y = \mu_0^{-1} \left(\frac{\partial B_x}{\partial z} - \frac{\partial B_z}{\partial x} \right)$$

$$J_z = \mu_0^{-1} \left(\frac{\partial B_y}{\partial x} - \frac{\partial B_x}{\partial y} \right) \quad (\text{A.4})$$

$$(\text{A.5})$$

where $\mu_0 = 4\pi \times 10^{-7} \text{ kg m s}^{-2} \text{ A}^{-2}$ is the magnetic permeability of free space and the magnetic fields are measured in T. The horizontal spatial derivatives are calculated using finite differences. The vertical derivatives are calculated using the inferred atmospheric parameters at different heights in the atmosphere. For this purpose, we fix 100 km as the target height for the disambiguation and then compute the vertical derivatives by interpolation at 90 and 100 km. The code is part of the `3DStokesFlow` package and is publicly available at <http://github.com/aasensio/3DStokesFlow>.